Physics of Plasmas

RESEARCH ARTICLE | MARCH 13 2026

# Topological and dynamic characteristics in forced anisotropic magnetohydrodynamic turbulence

Kai Gao ; Bin Jiang ; Cheng Li ; Yan Yang ; Kangcheng Zhou ; William H. Matthaeus ; Sean Oughton ; Minping Wan



*Phys. Plasmas* 33, 032304 (2026)
https://doi.org/10.1063/5.0311372

Physics of Plasmas ARTICLE pubs.aip.org/aip/pop

# Topological and dynamic characteristics in forced anisotropic magnetohydrodynamic turbulence

Cite as: Phys. Plasmas **33**, 032304 (2026); doi: 10.1063/5.0311372
Submitted: 9 November 2025 · Accepted: 26 February 2026 ·
Published Online: 13 March 2026



Kai Gao,[1,2] Bin Jiang,[3] Cheng Li,[1,2] Yan Yang,[4,a)] Kangcheng Zhou,[1,2] William H. Matthaeus,[4] Sean Oughton,[5] and Minping Wan[1,2,b)]

## AFFILIATIONS

[1]Guangdong Provincial Key Laboratory of Turbulence Research and Applications, Department of Mechanics and Aerospace Engineering, Southern University of Science and Technology, Shenzhen 518055, People's Republic of China
[2]Shenzhen Key Laboratory of Complex Aerospace Flows, Department of Mechanics and Aerospace Engineering, Southern University of Science and Technology, Shenzhen 518055, People's Republic of China
[3]School of Mechanical Engineering and Mechanics, Xiangtan University, Xiangtan 411105, People's Republic of China
[4]Department of Physics and Astronomy, University of Delaware, Newark, Delaware 19716, USA
[5]Department of Mathematics, University of Waikato, Hamilton 3240, New Zealand

[a)]Electronic mail: yanyang@udel.edu
[b)]Author to whom correspondence should be addressed: wanmp@sustech.edu.cn



## ABSTRACT

The invariants of the velocity gradient tensor in turbulence offer a compact description of local kinematics and flow topology. For incompressible magnetohydrodynamic turbulence, analysis of the second and third invariants ($Q$, $R$) of the velocity gradient tensor clarifies how coherent structures are organized and evolve. Extending the same analysis to the magnetic field gradient tensor provides additional information on the dynamics. In this study, pseudo-spectral simulation is used to obtain the velocity and magnetic field of the turbulent flow, and analysis of the flow field is conducted through joint probability density functions (PDFs) of the invariants. Furthermore, we explore the influence of the external mean magnetic field strength, $B_0$. The results show that when an external magnetic field is present, the $Q$–$R$ joint PDF no longer maintains the familiar teardrop distribution for the velocity field, and the flow field structure tends to be two-dimensional with increasing $B_0$. For the fluctuation magnetic field, the $Q$–$R$ joint PDF takes on a "cigar" shape that becomes more elongated as $B_0$ increases. Moreover, as the strength of the external mean magnetic field increases, the turbulence exhibits enhanced small-scale dissipation and localization, accompanied by a reduction in the effective dimensionality of the system toward a quasi-two-dimensional regime.



## I. INTRODUCTION

The evolution of the fluid velocity gradient tensor is crucial for understanding the kinematics and dynamics of turbulence, which has been investigated through a simplified Euler model by neglecting several unclosed terms in Refs. 1 and 2. The fluid velocity gradient tensor is related to elementary flow patterns, such as vorticity and shear, which are collectively referred to as flow topology. The flow topology can be analyzed and classified by the geometric invariants of the velocity gradient tensor, see, for example, Refs. 3–5. Studies of the invariants of the velocity gradient tensor for different types of hydrodynamic turbulence have led to a better understanding of small-scale features. Perhaps the most intriguing feature is the teardrop shape of the joint probability distribution function (PDF) of the second and third invariants of the velocity gradient tensor,[6–8] which is typically observed in both numerical simulations[9] and experiments.[10]

The velocity gradient tensor is defined as $\boldsymbol{A} = \nabla \boldsymbol{v}$ and has the characteristic equation $\lambda^3 + P_A\lambda^2 + Q_A\lambda + R_A = 0$,[11,12] where $\lambda$ is any eigenvalue of $\boldsymbol{A}$, and the coefficients $P_A$, $Q_A$, and $R_A$ are the first three invariants of $\boldsymbol{A}$. In the case of incompressible fluids, $P_A = -\mathrm{Tr}(\boldsymbol{A}) = 0$, where Tr represents the trace. The second and third invariants of $A_{ij}$ are

$$Q_A = -\frac{1}{2}A_{ij}A_{ji} = \frac{1}{4}\omega_i\omega_i - \frac{1}{2}S_{ij}S_{ij}, \tag{1}$$

$$R_A = -\frac{1}{3}A_{ij}A_{jk}A_{ki} = -\frac{1}{3}\mathrm{Tr}(\boldsymbol{S}^3) - \frac{1}{4}\omega_i\omega_j S_{ij}, \tag{2}$$

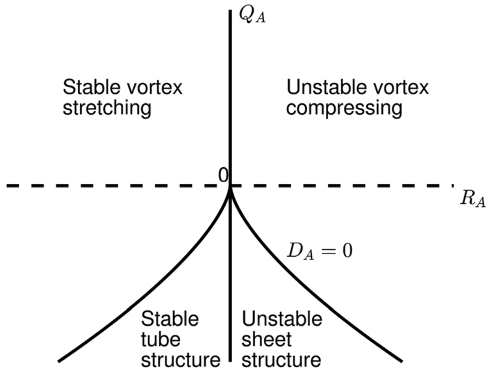


**FIG. 1.** Schematic of the partitioning of the $Q_A$–$R_A$ plane, where these are, respectively, the second and third invariants of the velocity gradient tensor $\nabla \boldsymbol{v}$. Topological types of structures found in the different regions are indicated.

where $\boldsymbol{\omega}$ is the vorticity and $S_{ij} = \frac{1}{2}(A_{ij} + A_{ji})$ is the strain rate tensor. The joint PDF of the invariants $Q_A$ and $R_A$, as illustrated in Fig. 1, allows the classification of various topologies.[13–15] $Q_A$ quantifies the competition between rotation and strain. $R_A$ contains two physically distinct contributions: strain self-amplification, represented by $-\frac{1}{3}\mathrm{Tr}(\boldsymbol{S}^3)$, and vortex stretching, represented by $-\frac{1}{4}\omega_i\omega_j S_{ij}$.[16] They are closely connected to inter-scale energy transfer in turbulence.[17] Moreover, vortex stretching can lead to the formation of extreme events,[18] and amplification of gradients is an essential component of the energy cascading process.[19,20]

The roots of the characteristic equation, i.e., the eigenvalues of $\boldsymbol{A}$, may be real or complex and are determined by the sign of the discriminant of $\boldsymbol{A}$, defined for incompressible flow as $D_A = \frac{R_A^2}{4} + \frac{Q_A^3}{27}$. The line $D_A = 0$, known as the Vieillefosse tail,[1,2,21] partitions the plane $(Q, R)$ into two regions with different features of the flow: one is elliptic for $D_A > 0$, and the other is hyperbolic for $D_A < 0$. When $R_A < 0$, the topology is stable, and, otherwise, for $R_A > 0$, it is unstable. Therefore, these two lines, $D_A = 0$ and $R_A = 0$, divide the $(Q, R)$ plane into four subregions, each corresponding to a different streamline pattern, i.e., a different flow topology. The four topological structures are as follows: (1) stable-focus-stretching (SFS), also known as vortex stretching for $D_A > 0$ and $R_A < 0$; (2) unstable-focus-compression (UFC), also known as vortex compressing for $D_A > 0$ and $R_A > 0$; (3) stable-node-saddle-saddle (SNSS), also known as tube structure for $D_A < 0$ and $R_A < 0$; and (4) unstable-node-saddle-saddle (UNSS), also known as sheet structure for $D_A < 0$ and $R_A > 0$.[22–26]

In hydrodynamic turbulence, the joint PDF of $(Q_A, R_A)$ exhibits a generic feature, that is, it has a characteristic inclined teardrop shape. This has been observed in the boundary layer,[27,28] shear flow,[29] channel flow,[30] and even in compressible turbulence simulations,[31] which will also be illustrated in Fig. 4(a). The teardrop shape is elongated in the second and fourth quadrants, and its tip is located along the $D_A = 0$ branch. This is suggestive that the turbulent structures favor vortex stretching and sheet structures. Note that in many visualizations of hydrodynamic turbulence, the vortex structure appears to be tubular, but there are sheets between these vortex tubes, where most of the dissipation is located in these sheets.[32,33]

The velocity gradient tensor $\boldsymbol{A} = \nabla \boldsymbol{v}$ can be decomposed into index symmetric and antisymmetric parts

$$A_{ij} = \partial_i v_j = S_{ij} + W_{ij}, \tag{3}$$

where $W_{ij} = \frac{1}{2}(A_{ij} - A_{ji})$ denotes the rotation rate tensor. Similarly, we can obtain their respective second and third invariants

$$Q_S = -\frac{1}{2} S_{ij} S_{ji} \quad \text{and} \quad R_S = -\frac{1}{3} S_{ij} S_{jk} S_{ki}, \tag{4}$$

$$Q_W = -\frac{1}{2} W_{ij} W_{ji}. \tag{5}$$

Note that the third invariant of $W_{ij}$, $R_W$, is zero due to the antisymmetry of $W_{ij}$.

The $(Q_S, R_S)$ joint PDF characterizes the geometry of the local strain in the fluid element, as shown in Fig. 2. The second invariant $Q_S$ is negative definite because $S_{ij}$ is symmetric. One can also derive that $D_S = \frac{R_S^2}{4} + \frac{Q_S^3}{27} \leq 0$ and therefore the $(Q_S, R_S)$ joint PDF, as illustrated in Fig. 2, can only be nonzero in the region beneath the $D_S = 0$ line. When $R_S > 0$, two of the eigenvalues of $S_{ij}$ are positive, and the third one is negative, which is therefore associated with sheet structures. Similarly, $R_S < 0$ is associated with tubular structures. Proximity to the $R_S = 0$ axis indicates that the flow field structure is closer to being two-dimensional.[34,35]

The $(Q_W, -Q_S)$ joint PDF (Fig. 3) determines the relative importance of strain vs rotation. Note that $Q_S$ and $Q_W$ are in direct association with viscous dissipation $\varepsilon_\nu = 2\nu S_{ij} S_{ij} = -4\nu Q_S$ and enstrophy

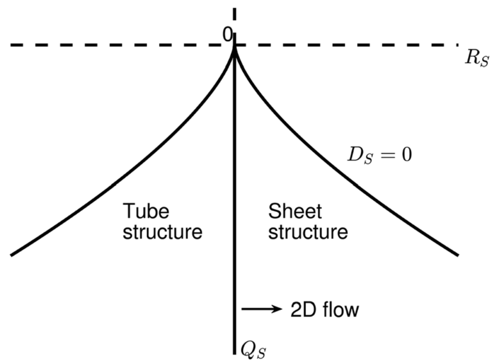


**FIG. 2.** Schematic of the partitioning of the $Q_s$–$R_s$ plane associated with the second and third invariants of the strain rate tensor $S_{ij}$. Topological types of structures found in the different regions are indicated.

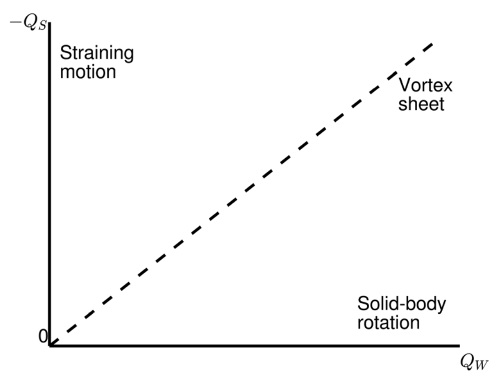


**FIG. 3.** Schematic of the partitioning of the $Q_s$–$Q_W$ plane, where these are the second invariants of the strain rate tensor ($S$) and the rotation rate tensor ($W$).

$\Omega = \frac{1}{2}\omega^2 = 2Q_W$, respectively. Patterns near the $-Q_S$ axis reflect (almost) pure strain motion, i.e., regions with strong dissipation but negligible enstrophy. Patterns near the $Q_W$ axis are (almost) pure solid rotations with high enstrophy but very weak dissipation and tend to be concentrated in tubular structures. Regions with comparable strain and rotation rates, i.e., near the $Q_W = -Q_S$ line, correspond to vortex sheets.[22,36]

Similar categorization can be applied to magnetohydrodynamic (MHD) turbulence, which is, however, more complicated than its hydrodynamic counterpart because of the coupling of velocity and magnetic fields. In analogy with the velocity field, we can also obtain the corresponding invariants of the magnetic field gradient tensor $\boldsymbol{X} = \nabla \boldsymbol{b}$ and its symmetric $K_{ij} = \frac{1}{2}(X_{ij} + X_{ji})$ and antisymmetric $J_{ij} = \frac{1}{2}(X_{ij} - X_{ji})$ parts

$$Q_X = -\frac{1}{2}X_{ij}X_{ji} \quad \text{and} \quad R_X = -\frac{1}{3}X_{ij}X_{jk}X_{ki}, \tag{6}$$

$$Q_K = -\frac{1}{2}K_{ij}K_{ji} \quad \text{and} \quad R_K = -\frac{1}{3}K_{ij}K_{jk}K_{ki}, \tag{7}$$

$$Q_J = -\frac{1}{2}J_{ij}J_{ji}. \tag{8}$$

Examining the joint PDF of $Q_K$ and $R_K$, we can study the geometry of the local magnetic strain. The $(Q_J, -Q_K)$ joint PDF describes the relative importance between the strain and rotational portions of the magnetic field gradient, similar to $(Q_W, -Q_S)$ of the velocity gradient. An important difference is that the Ohmic dissipation $\varepsilon_b = \eta j^2 \propto Q_J$ is directly related to the rotational portion $J_{ij}$, rather than the strain portion $K_{ij}$.[37,38]

MHD is significant in engineering and also in astrophysics, where it plays a pivotal role in elucidating the dynamics of the solar system and the star formation process.[39] A large amount of work in incompressible MHD turbulence has primarily concentrated on intermittency, scaling properties, and isotropy.[40–43] There has been a paucity of research conducted on the small-scale structure of MHD turbulence, which is closely associated with dissipation and the topology of turbulence. In this context, a systematic investigation of the gradient tensors of magnetic and velocity fields and their invariants can provide valuable insights.

Following the studies in HD turbulence, Dallas and Alexakis[22] use direct numerical simulation (DNS) to study the small-scale topological and dynamical characteristics of decaying MHD turbulence with different large-scale initial conditions. Their results show that in contrast to the universal teardrop in HD turbulence, each MHD flow has a different shape for the joint $(Q_A, R_A)$ PDF of the velocity gradient. The structures and dynamics at the time of maximum dissipation depend on the large-scale initial conditions as well. Sahoo *et al.*[44] report that, at large $Pr_M$, the magnetic field is more intermittent than the velocity field, whereas at small $Pr_M$, the trend reverses. In a subsequent study employing random power-law forcing, they again find enhanced magnetic intermittency at large $Pr_M$ and show that such forcing can markedly modify the morphology of coherent structures.[45]

Analogous study on the statistics of the velocity and magnetic gradient tensor was first carried out in space plasma turbulence.[46] Before the Cluster mission,[47] multi-spacecraft data were inaccessible, precluding computation of the full gradient. Consolini *et al.*[46] and Quattrociocchi *et al.*,[11] using the Cluster data in the magnetosheath and solar wind, analyze the coarse-grained velocity and magnetic field gradient tensors to characterize the features of the magnetic and velocity field structures. The results show that the joint PDF of the velocity gradient invariants $(Q_A, R_A)$ is remarkably similar to that observed at the lower end of the inertial range of fluid turbulence. In particular, there is evidence for a significant increase in the joint statistics along the so-called Vieillefosse tail, which supports dissipation or dissipation production due to vortex stretching. Further analyses in Ref. 11 show that the joint statistics of magnetic-gradient invariants depend strongly on the ratio $R = L/\eta_{\mathrm{p}}$, where $L$ is the characteristic scale and $\eta_{\mathrm{p}}$ is the proton inertial length. This scale dependence appears consistent with a transition in the fluctuation-field dimensionality from quasi-2D at large scales to nearly 3D at small scales close to $\eta_{\mathrm{p}}$.

Hnat *et al.*[48] use multipoint observations from the European Space Agency (ESA) Cluster mission to examine the magnetic field topology of coherent structures in the solar wind. Their analysis shows that magnetic reconnection, together with turbulent interactions, plays a crucial role in converting magnetic energy into plasma heating and dissipation. Yang *et al.*[49,50] and Bandyopadhyay *et al.*[51] use the symmetric/antisymmetric parts of the magnetic and velocity field gradient tensors to quantify the kinetic dissipation in turbulent space plasmas at sub-ion scales in the Earth's magnetosheath using Magnetospheric Multiscale (MMS) spacecraft data. These studies show how dissipation is clearly localized near strong current sheets.

Zhang *et al.*[52] analyze high-resolution MMS measurements in the Earth's magnetosheath and find that dissipation at kinetic scales is mainly controlled by sheet-like structures, where the straining and rotational components of the magnetic and velocity gradients are strongly correlated. Building on this framework, Quattrociocchi *et al.*[53] derive evolution equations for the velocity- and magnetic field gradient invariants. Their analysis indicates that the balance between magnetic and hydrodynamic effects differs between the solar wind and magnetosheath, marking distinct turbulent regimes. Using a similar topological approach, Huang *et al.*[54] establish a clear correspondence between field topology and dissipation. Extending these findings, Xiong *et al.*[55] employ particle-in-cell simulations and MMS observations to show that a stronger guide field favors the generation of O-type topology ($D_X = \frac{R_X^2}{4} + \frac{Q_X^3}{27} > 0$) and increases energy conversion efficiency, suggesting that the mean magnetic field regulates turbulence-driven dissipation during reconnection.

In the context of 3D MHD turbulence, the study of topology primarily concentrates on incompressible, isotropic, and decaying turbulence. However, there has been less study of topology in more general types of MHD turbulence, such as in the presence of compressibility or anisotropy. In the latter case, application of an external mean magnetic field results in the turbulent fields becoming anisotropic and vortex structures transition from a disordered state to an ordered state with increase in the applied magnetic field.[56] Evidently, the study of the evolution of the topological structure in this transition is a useful undertaking.

In this paper, an attempt is made to gain insight into the universal and non-universal features of MHD turbulence by studying the structures and dynamics of small scales through joint PDFs of the invariants of the velocity gradient, magnetic field gradient, and related tensors. An emphasis is placed on effects of anisotropy induced by an external applied magnetic field of varying strengths. Through this analysis, a classification of the structures in MHD turbulence is also attempted. The organization of the paper is as follows. Section II describes numerical methods, initial conditions, and DNS parameters. Section III describes the joint PDF analysis of gradient tensor invariants associated with velocity and magnetic fields. Finally, the Conclusion section summarizes results pertinent to the structure and dynamics of MHD turbulence.

## II. NUMERICAL METHODS

The governing equations for the simulation of externally driven incompressible MHD turbulence are

$$\frac{\partial \boldsymbol{v}}{\partial t} + (\boldsymbol{v}\cdot\nabla)\boldsymbol{v} = -\nabla\left(p + \frac{|\boldsymbol{b}+\boldsymbol{B_0}|^2}{2}\right) + (\boldsymbol{b}\cdot\nabla)\boldsymbol{b} + (\boldsymbol{B_0}\cdot\nabla)\boldsymbol{b} + \nu\nabla^2\boldsymbol{v} + \boldsymbol{f}_v, \quad (9)$$

$$\frac{\partial \boldsymbol{b}}{\partial t} + (\boldsymbol{v}\cdot\nabla)\boldsymbol{b} = (\boldsymbol{b}\cdot\nabla)\boldsymbol{v} + (\boldsymbol{B_0}\cdot\nabla)\boldsymbol{v} + \eta\nabla^2\boldsymbol{b}, \quad (10)$$

$$\nabla\cdot\boldsymbol{v} = 0, \quad (11)$$

$$\nabla\cdot\boldsymbol{b} = 0, \quad (12)$$

where the velocity and magnetic fluctuations are denoted by $\boldsymbol{v}$ and $\boldsymbol{b}$, respectively. The magnetic field is expressed in Alfvén-speed units, i.e., scaled by $\sqrt{4\pi\rho}$ with $\rho$ being the uniform mass density. An external mean magnetic field $\boldsymbol{B_0} = B_0\boldsymbol{e_z}$ is imposed along the $z$ axis of a Cartesian domain $(x, y, z)$, and its amplitude is measured relative to the rms magnetic fluctuation ($b_{\mathrm{rms}} \approx 1$) in the initial state. The thermal pressure is written as $p$, while $\nu$ and $\eta$ represent the kinematic viscosity and the magnetic diffusivity, respectively.

To sustain a statistically steady turbulent regime, a divergence-free forcing term $\boldsymbol{f}_{\boldsymbol{v}}$ is introduced into the momentum equation. The forcing is applied at the largest scales (i.e., the first two wavenumber shells $k = 1$ and $k = 2$) and injects energy at a fixed rate following a Gaussian, $\delta$-correlated random process.[57]

The computations are performed in a cube of size $[0, 2\pi]^3$ with periodic boundary conditions. The governing equations are solved using a pseudo-spectral solver with de-aliasing by the two-thirds rule and advanced in time with a second-order Adams–Bashforth scheme. All simulations are started from random velocity and magnetic fluctuations confined to the low-wavenumber range $1 \le k \le 5$. The corresponding initial spectra follow $E(k) \propto [1 + (k/k_0)]^{-11/3}$ with $k_0 = 3$, which sets the spectral knee. The initial magnetic and kinetic energies are equally partitioned ($E_v = E_b = 0.5$), with (almost) vanishing cross helicity, and all runs employ equal viscosity and resistivity to maintain a unit magnetic Prandtl number.

We investigate the topological and dynamic characteristics of forced anisotropic incompressible MHD turbulence under varying intensities of an external mean magnetic field, $B_0$. The simulation parameters are summarized in Table I. All runs are carried out on a $1024^3$ grid using a viscosity of $\nu = \eta = 8 \times 10^{-4}$. The numerical resolution satisfies $k_{\max}\eta_{k,v} > 1.5$, where the Kolmogorov length scale is defined as $\eta_{k,v} = (\nu^3/\varepsilon_v)^{1/4}$ with $\varepsilon_v$ denoting the kinetic energy dissipation rate. The simulation setup follows the method described in Ref. 56.

**TABLE I.** Summary of the simulation parameters under different strengths of the external mean magnetic field ($B_0$), as determined after statistically steady states are reached. The quantities $\varepsilon_v$ and $\varepsilon_b$ denote, respectively, the kinetic and magnetic energy dissipation rates, and $b_{\mathrm{rms}}$ is the rms magnetic fluctuation amplitude. The kinetic and magnetic Taylor-scale Reynolds numbers are denoted by $R_{\lambda,v}$ and $R_{\lambda,b}$, respectively. The parameter $k_{\max}\eta_{k,v}$ is used to evaluate the numerical resolution, where $\eta_{k,v}$ is the Kolmogorov length scale and $k_{\max}$ corresponds to the highest resolved wavenumber (equal to one-third of the grid number in a single direction).

| Run | $B_0$ | Grids | $\varepsilon_v$ | $\varepsilon_b$ | $b_{\mathrm{rms}}$ | $R_{\lambda,v}$ | $R_{\lambda,b}$ | $k_{\max}\eta_{k,v}$ |
|---|---|---|---|---|---|---|---|---|
| $W1$ | 0 | $1024^3$ | 0.59 | 1.39 | 0.88 | 290 | 89 | 1.86 |
| $W2$ | 2 | $1024^3$ | 0.78 | 1.07 | 1.11 | 295 | 164 | 1.73 |
| $W3$ | 5 | $1024^3$ | 0.81 | 0.80 | 1.02 | 467 | 166 | 1.71 |

## III. NUMERICAL RESULTS

The dissipative three-dimensional incompressible MHD turbulence eventually reaches a statistically steady state in the presence of an external force $\boldsymbol{f}_v$. Different external mean magnetic fields $\boldsymbol{B}_0$ are applied along the $z$-direction to study the effects on the topological structure of the velocity field and the magnetic field. Recall that the initial magnetic fluctuations have $b_{\mathrm{rms}} \sim 1$ in all cases. As expected, anisotropy increases with increasing external magnetic field.[58] Furthermore, increasing $B_0$ leads to a decrease in the relative strength of the nonlinear coupling and a reduction in the maximum values of vorticity and current density, thus suppressing but not eliminating the development of turbulence.[59] In this section, we present results from the joint PDF analysis of the gradient tensor invariants characterizing the velocity and magnetic fields. All PDFs are calculated using data from the steady-state periods of the simulations. For each $B_0$, the $\nabla\boldsymbol{v}$ and $\nabla\boldsymbol{b}$ based PDFs are calculated at the same instant.

### A. The topology of the velocity field

The joint PDF of the second and third invariants of the velocity gradient tensor, $Q_A$ and $R_A$, is shown in Fig. 4, for cases with varying values of $B_0$. The color scale indicates the logarithmic values of the probability density. For the run with no external mean magnetic field, it can be seen that the joint PDF of the second and third invariants is a standard teardrop configuration. However, in cases with an external magnetic field, the joint distributions of $Q_A$ and $R_A$ no longer maintain the same teardrop shape. In particular, with increasing $B_0$, the "tail" along the zero-discriminant line $D_A = 0$ becomes less pronounced, and the distribution becomes more symmetric about the $R_A = 0$ axis, since extreme events predominantly occur in the tail of the joint PDF and are driven by vortex stretching. These trends suggest that velocity gradient intermittency tends to weaken as the external mean magnetic field increases. When $Q_A$ is large and negative, the local strain is high, which is unfavorable to the formation of vortices. On the contrary, when $Q_A$ is large and positive, the vorticity dominates. As the external magnetic field increases, it becomes less probable to find large values of $Q_A$ and $R_A$, i.e., regions of large strain and large vorticity are suppressed.

As shown in Table II, irrespective of the magnitude of the external mean magnetic field, the region dominated by vortex stretching is larger than that associated with vortex compression in all three runs. Similarly, the sheet structure is found to be more commonplace than the tube structure. The percentage of area dominated by the vortex stretching region (SFS) decreases as the external mean magnetic field increases. When $B_0 = 0$, the SFS region accounts for 39.0% of the area, and when $B_0$ increases to 5, the SFS region is reduced to 35.7% of the area. Nevertheless, the area of SFS domination continues to exceed the area of vortex compression.

The proportion of the vortex compression region (UFC) declines (slightly) in conjunction with the augmentation of the external mean magnetic field. The proportion of the tube structure region (SNSS) increases with the increase in the external mean magnetic field. The proportion of the sheet structure region (UNSS) increases very slightly with the increase in the external mean magnetic field.

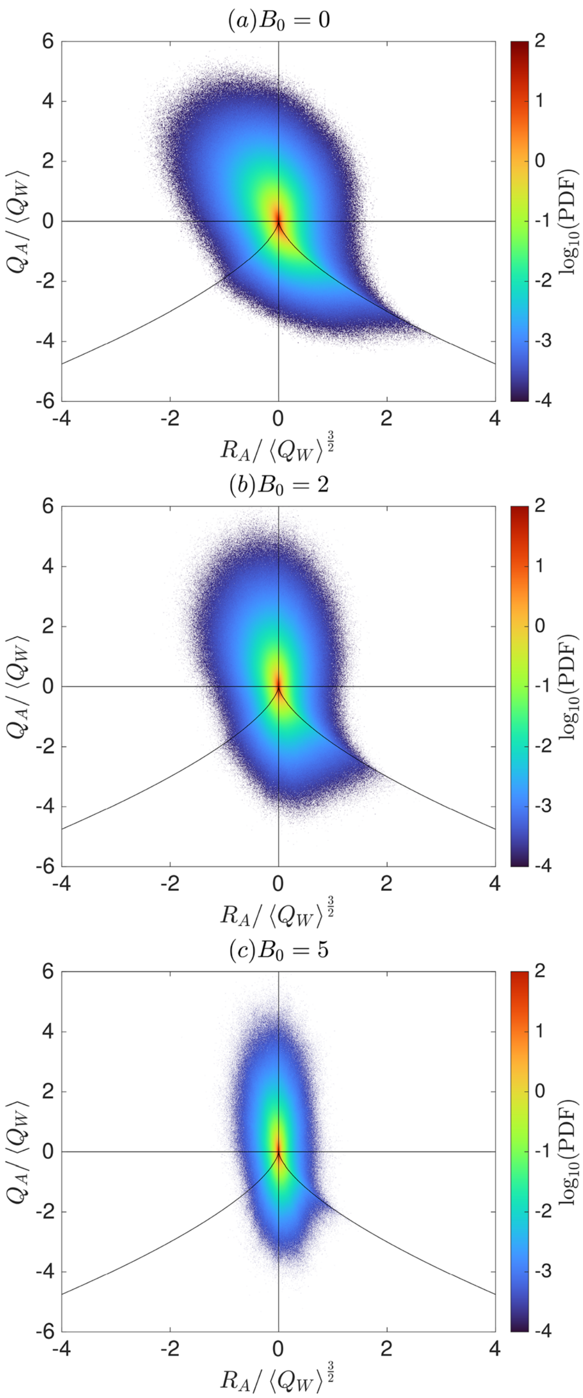


FIG. 4. Joint PDFs of the second and third invariants $(Q_A, R_A)$ of the velocity gradient tensor $A_{ij}$, normalized by appropriate powers of the mean enstrophy $\langle Q_W \rangle$.

Figure 5 shows the joint distribution function of the second and third invariants of the symmetric strain tensor, $R_S$, and $Q_S$, for different values of external magnetic fields. With the increase in the external magnetic field, the data distribution shifts closer to the $R_S = 0$ line, indicating that the structure of the flow field gets closer to a quasi-two-dimensional structure. This behavior is a guide-field-constrained statistically steady state (quasi-relaxed state) established by the balance between forcing and dissipation. Turbulent relaxation and self-organization in fluids and plasmas have been discussed from complementary viewpoints, including dynamical principles based on entropy production.[60] More recently, Banerjee *et al.*[61] propose the principle of vanishing nonlinear transfer (PVNLT), which provides a unified pathway to turbulent relaxed states encompassing both aligned (Beltrami/Alfvénic-type) states and more general pressure-supported/pressure-balanced relaxed configurations. Although PVNLT is formulated for relaxation after quenching the drive, its central idea—that strong constraints can deplete nonlinear transfers and thereby favor more organized states—offers a useful perspective for interpreting guide-field-regulated MHD turbulence in statistically steady conditions.

TABLE II. Proportions of velocity field topology types under different external mean magnetic field strengths. (Note that the values are rounded, so the total may not be exactly 100%.)

| | $B_0 = 0$ | $B_0 = 2$ | $B_0 = 5$ |
|---|---|---|---|
| Vortex stretching (SFS) | 39.0% | 37.1% | 35.7% |
| Vortex compression (UFC) | 31.8% | 31.0% | 29.6% |
| Tube (SNSS) | 9.5% | 12.0% | 13.7% |
| Sheet (UNSS) | 19.7% | 19.9% | 20.9% |

In fact, the solar wind exhibits certain quasi-two-dimensional characteristics.[58,62] At heliocentric distances around $\sim 1$ AU, Bieber *et al.*[63] show that magnetic field fluctuations are well described by a slab + 2D superposition, with the 2D contribution being dominant. Closer to the Sun, recent measurements further suggest that both the anisotropy and the relative slab/2D weights vary with heliocentric distance and with solar-wind conditions.[64,65] In this regard, the present results appear to be consistent with the observational data. The probability of larger negative values of $Q_S$ increases as $B_0$ increases, resulting in an increasing number of small-scale structures with high dissipation. Furthermore, calculating the relevant areas in the figure reveals that the proportion of $R_S > 0$ is greater, which is related to the sheet structure of the flow field. We may conclude that a larger fraction of dissipation occurs in sheet-like structures.

To the same point, Fig. 6 shows the joint density distribution function of $(Q_W, -Q_S)$ at different external magnetic field strengths. It is apparent that as $B_0$ increases, the joint PDF becomes more closely concentrated near the line $Q_W = -Q_S$, again indicative of dissipation concentration in sheet-like structure, as depicted in Fig. 3.

## B. The topology of the magnetic field

For the magnetic field, we see in Fig. 7 that the joint PDF of the second and third invariants of the magnetic field gradient tensor, $Q_X$ and $R_X$, is cigar-shaped and nearly symmetric, although the details vary with $B_0$. With an increase in the external magnetic field, its shape becomes elongated, and the relative probability of large $Q_X$ values increases.

In Table III, the current tube stretching region is identified as the upper left quadrant of the $Q_X$, $R_X$ joint PDF and is the analog of the SFS for the velocity. It is evident from the data that the percentage of

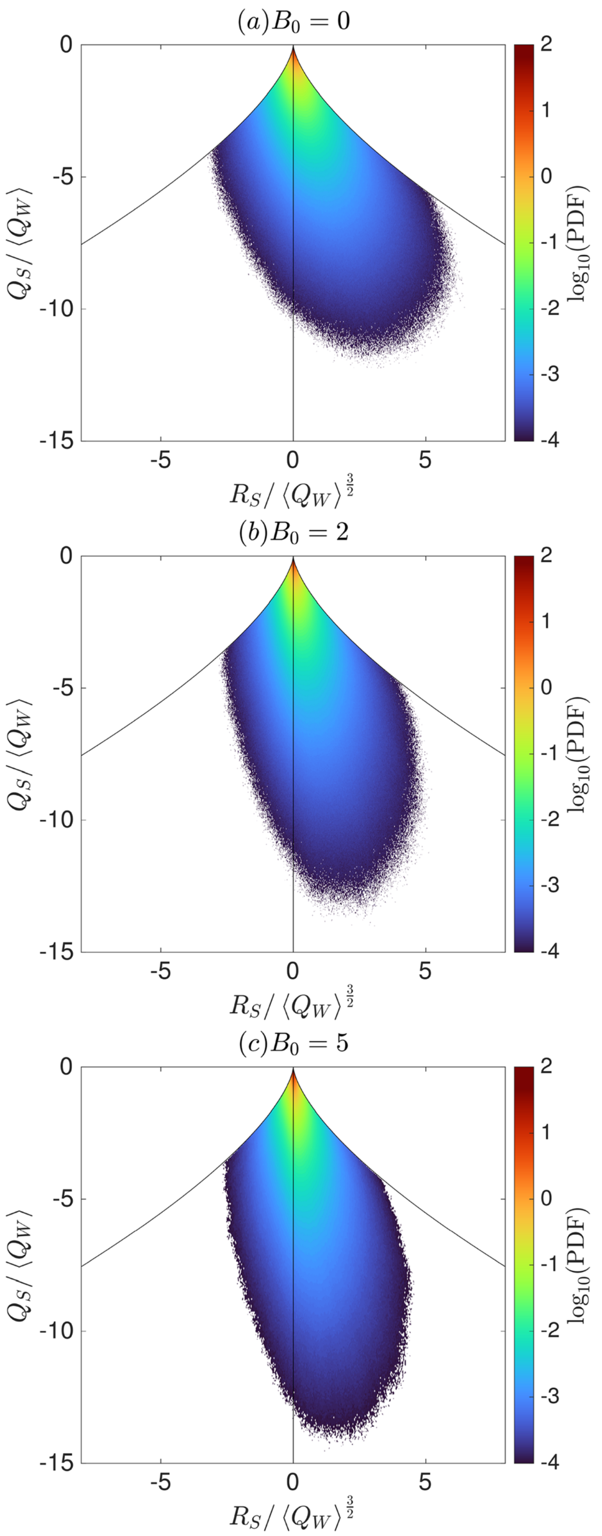


FIG. 5. Joint PDFs of the second and third invariants $(Q_S, R_S)$ of the strain rate tensor $S_{ij}$, normalized by appropriate powers of the mean enstrophy $\langle Q_W \rangle$.

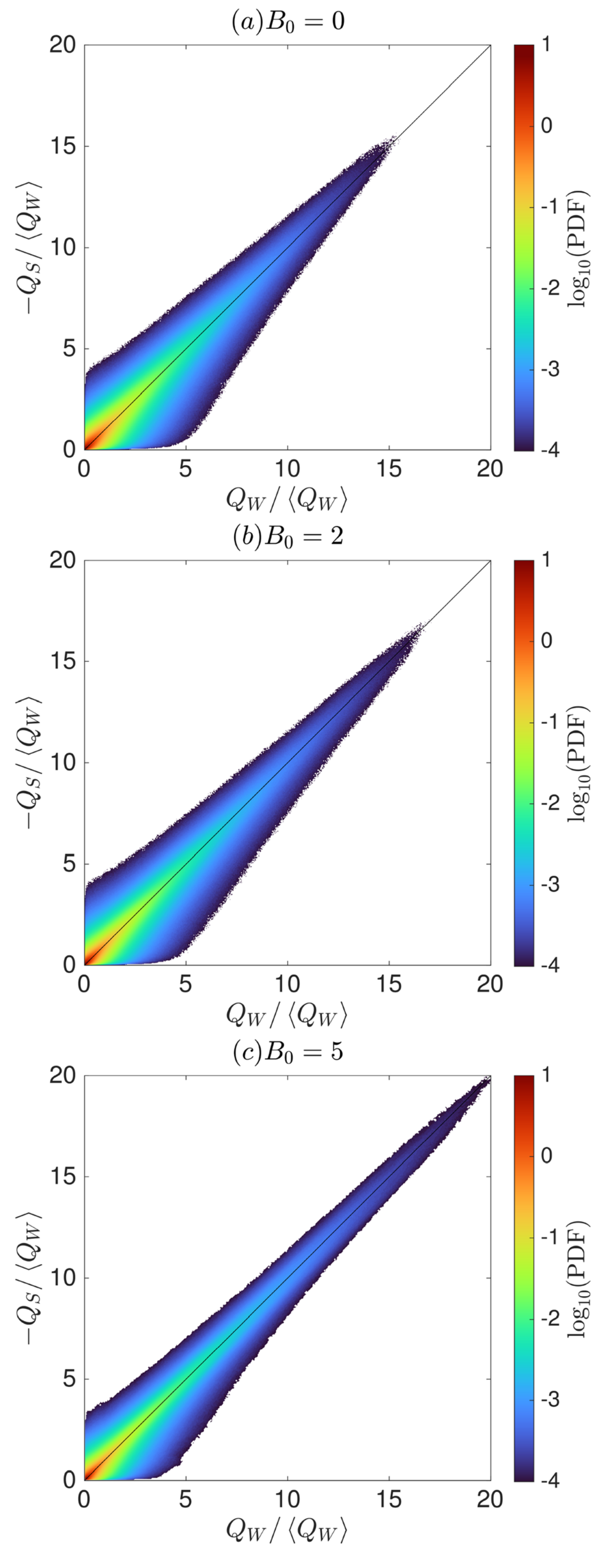


FIG. 6. Joint PDFs of the second invariant $Q_S$ of $S_{ij}$ and the second invariant $Q_W$ of $W_{ij}$, normalized by the mean enstrophy $\langle Q_W \rangle$. Recall $\partial_i v_j = S_{ij} + W_{ij}$.

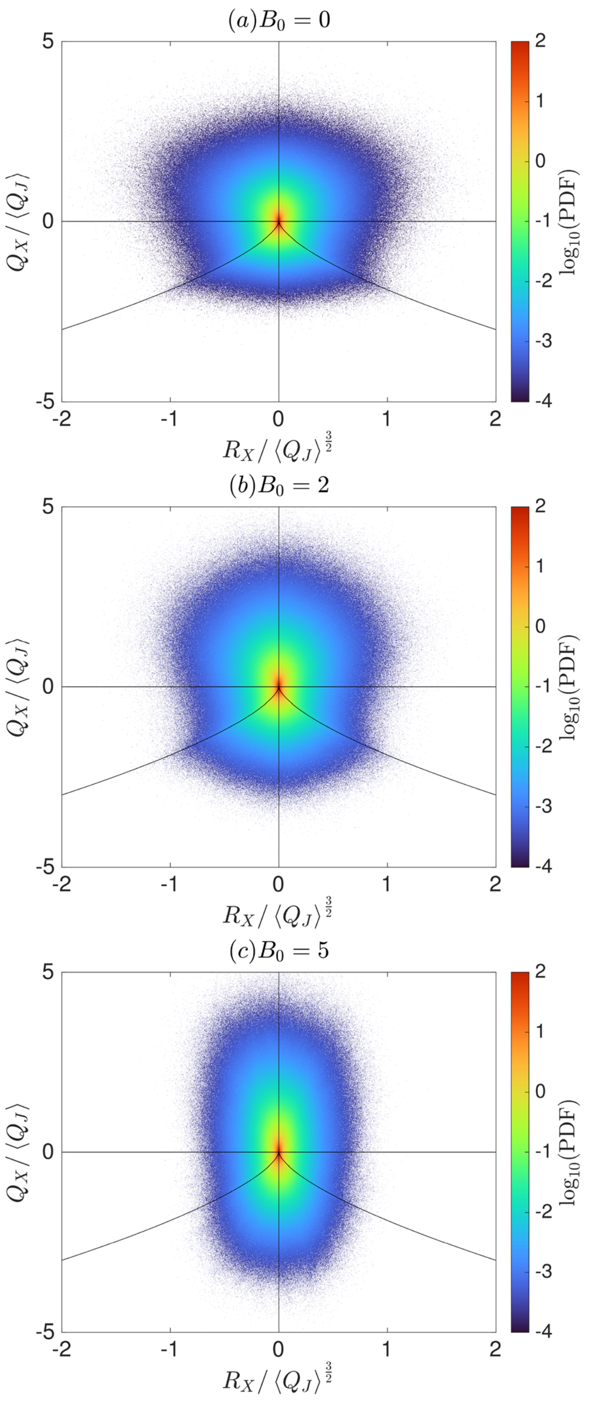


FIG. 7. Joint PDFs of the second and third invariants $(Q_X, R_X)$ of the magnetic-gradient tensor $X_{ij} = \partial_i b_j$, normalized by appropriate powers of $\langle Q_J \rangle$.

points in this current tube stretching region decreases (slightly) with an increase in the external mean magnetic field. Similarly, an increase in $B_0$ results in a slight decrease in the percentage of area in the current tube compression region (upper right, analog of UFC for the velocity).

**TABLE III.** Proportions of magnetic field topology types under different external mean magnetic field strengths.

| | $B_0 = 0$ | $B_0 = 2$ | $B_0 = 5$ |
|---|---|---|---|
| SFS | 35.5% | 34.1% | 32.7% |
| UFC | 35.4% | 34.0% | 32.8% |
| SNSS | 14.6% | 15.9% | 17.2% |
| UNSS | 14.6% | 16.1% | 17.2% |

On the other hand, an increase in $B_0$ leads to increases in the percentage of points in the regions associated with (i) tubular current structure (lower left, analog of SNSS for the velocity) and (ii) current sheets (lower right, analog of UNSS for the velocity). Considering the current tube and current sheet regions collectively, their percentage area increases with increasing $B_0$. Overall, we see that the $Q_X, R_X$ joint distribution for the magnetic field is much more symmetric than the $Q_A, R_A$ distribution for the velocity field, in agreement with Dallas and Alexakis.[22]

As the external magnetic field increases, the velocity field progressively becomes more two-dimensional (see Fig. 5), which is markedly different from the behavior of the magnetic field. The sequence of plots in Fig. 8 indicates that the structure of the three-dimensional magnetic field approaches a quasi-two-dimensional state at all values of $B_0$. In fact, in this regard, the influence of $B_0$ on the magnetic field fluctuations is ostensibly not significant. As shown in Fig. 9, as the external magnetic field increases, the ratio of its rotational part to the magnetic strain part changes little and remains in a configuration identified with two-dimensional sheet-like structure, revealing that Ohmic dissipation occurs in current sheets.[11,22,37] This is quite similar to the joint distribution of $(Q_W, -Q_S)$ of the velocity field, except that the dispersion around the line $Q_W = -Q_S$ is greater. This indicates that the current is closer to a sheet-like character than the vorticity at all values of the external mean magnetic field.

## IV. CONCLUSION

This paper has examined the topology of the velocity and magnetic fields in MHD turbulence with the main goal of understanding the influence of an externally applied mean magnetic field. The methodology is based on the examination of the joint distribution of the geometric invariants of the respective gradient tensors.[1–4] We find that with an external mean magnetic field, the velocity (Q,R) joint PDF no longer maintains the tear-drop type distribution that is familiar in hydrodynamics. Instead, as the external magnetic field increases, this distribution gradually tends to be symmetric, with less pronounced teardrop shape.

With the increase in the external magnetic field, the probability of finding large values of $Q_A$ and $R_A$ decreases, i.e., strong vorticity and strain in the region are suppressed; see Fig. 4. By comparing the percentage of structure in each part of the joint distribution (as diagramed in Fig. 1), it is found that the presence of tubular structure increases, as does the sheet structure, the latter less significantly.

Turning to the classification of properties based on the symmetric strain tensor (see Fig. 2), we find that generally speaking, the structure of the velocity field gets closer to a quasi-two-dimensional structure as the external magnetic field increases,[59] as shown in Fig. 5. At the same

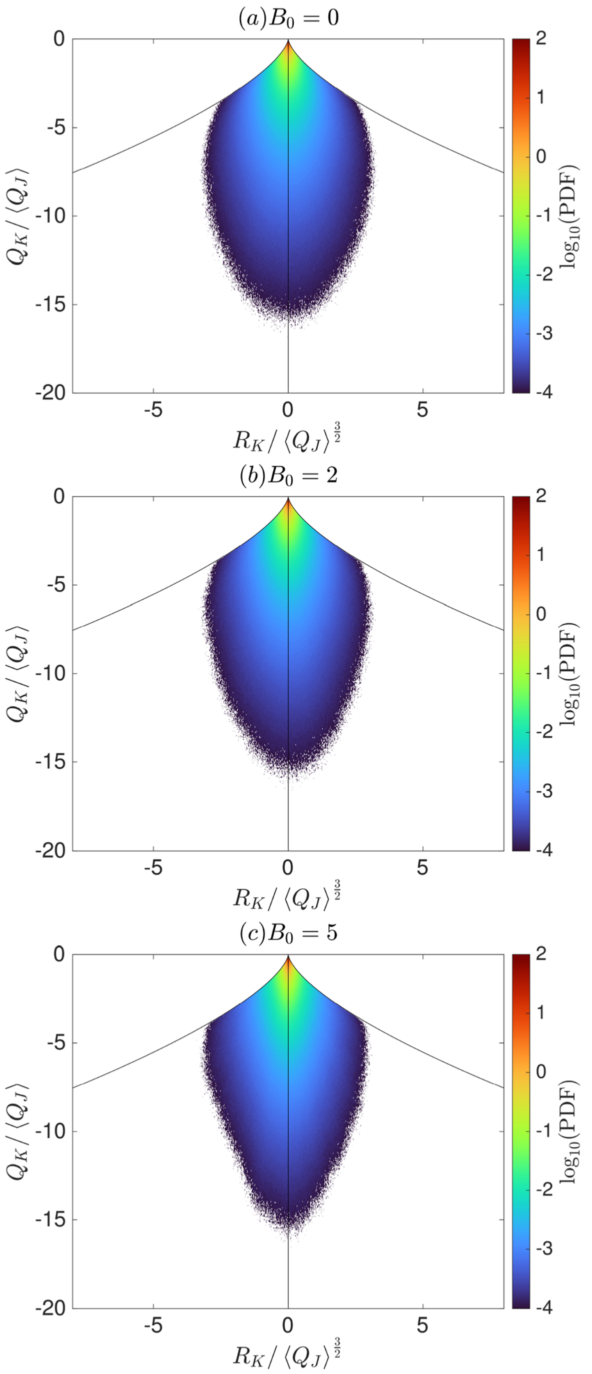


FIG. 8. Joint PDFs of the second and third invariants $(Q_K, R_K)$ of $K_{ij}$, normalized by appropriate powers of $\langle Q_J \rangle$. Recall $X_{ij} = \partial_i b_j = K_{ij} + J_{ij}$.

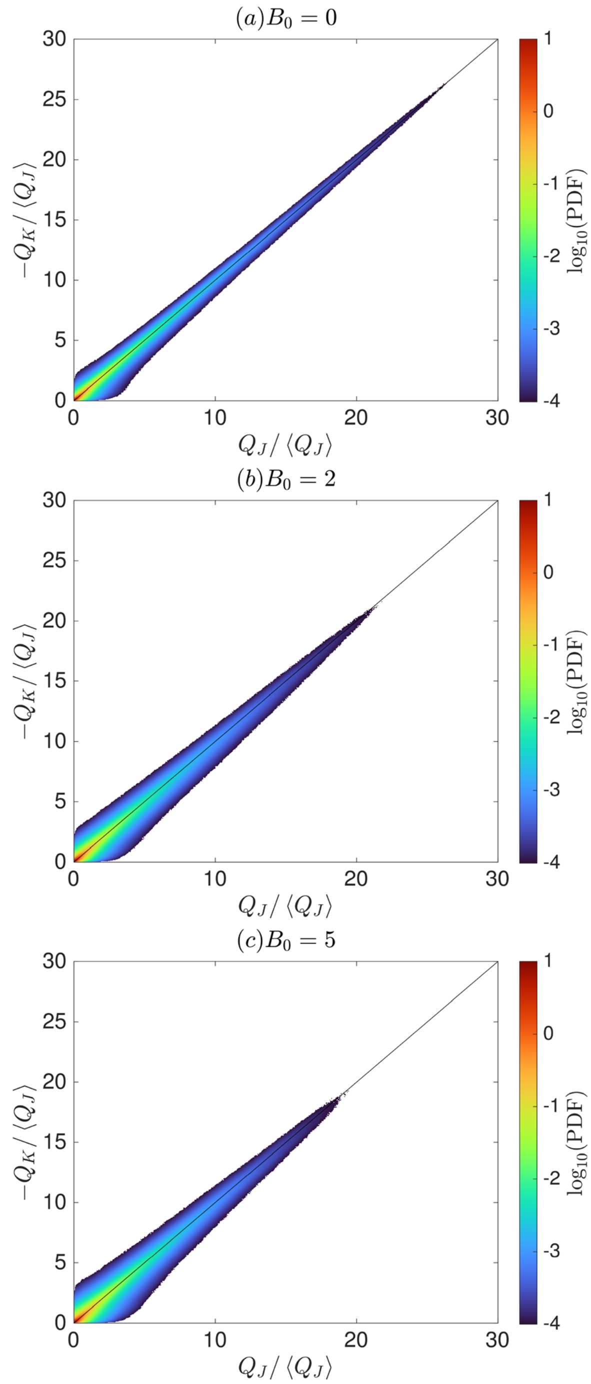


FIG. 9. Joint PDFs of the second invariant $Q_K$ of $K_{ij}$ and the second invariant $Q_J$ of $J_{ij}$, normalized by $\langle Q_J \rangle$.

time, the probability of larger negative values of $Q_S$ relative to average $Q_W$ increases with increasing external field, as is also evident in Fig. 5.

The overall picture appears to be that the system approaches a two-dimensional state with increasing $B_0$. It is well known that in the 2D limit of incompressible hydrodynamics, the enstrophy (mean square vorticity) becomes an ideal invariant and cannot be readily amplified, due to the absence of vortex stretching in the reduced dimensionality. This provides a rationale for reduction in the intensity of the vorticity in the $Q_A$, $R_A$ distribution. Likewise, two-dimensionality in MHD implies that vorticity will concentrate into (typically quadrupolar) structures, generally associated with magnetic reconnection sites (see Ref. 66). This effect is closely associated with filamentation of electric current density, discussed later.

We may also note that the population of points with $R_S > 0$ associated with the sheet-like structure remains larger than that associated with tube-like structure at all values of the mean field that we used. Thus, for the velocity field, viscous dissipation is found to be related to sheet-like structures, an effect increasing with increasing mean magnetic field strength.

For the magnetic field, the joint distribution function of the second and third invariants of the magnetic-gradient tensor, $R_X$ and $Q_X$, is cigar-shaped and more symmetric than the corresponding joint distribution for the velocity field. With the increase in the external magnetic field, its shape becomes elongated, and the probability of larger values of $R_X$ and $Q_X$ rises. It is found that the tubular structure is increased in relation to the sheet structure, by comparing the percentage of the structure in each part. The structure of the three-dimensional magnetic field in all cases approximates a quasi-two-dimensional condition, and the external magnetic field has little effect. This possibly surprising result is apparently due to emergence of local anisotropy relative to the local mean magnetic field direction.[67,68] Such local anisotropy must originate in dynamical effects described by statistical measures higher than second order.[69]

These findings are consistent with prior analyses that show the development of anisotropy as the external mean magnetic field increases.[58,59,70] Prior studies have usually focused on the anisotropic nature of the spectrum. Here, we have instead probed the topology of the turbulence and have examined the similarities and differences of the tensor invariants in MHD and in hydrodynamics, emphasizing how mean magnetic field differently influences the velocity and the magnetic topology in driven MHD turbulence. It remains to be seen whether the findings presented here become applicable to observations in the laboratory or in space plasmas, or whether variation in the nature of forcing may have additional influences.

Here, we focus on approximately balanced turbulence with nearly vanishing normalized cross helicity $\sigma_c \equiv \frac{2\langle \boldsymbol{v}\cdot\boldsymbol{b}\rangle}{\langle v^2\rangle+\langle b^2\rangle} \approx 0$. Nonzero cross helicity (Alfvénic imbalance) is known to reduce the effective strength of nonlinear interactions[59,71] and may suppress the production of extreme gradients; consequently, it can modify the tails and asymmetry of the joint PDFs of gradient invariants and the associated topology fractions. A systematic exploration of the $\sigma_c$ dependence will be pursued in future work. Similarly, we set the magnetic Prandtl number to unity in our simulations. However, $Pr_M$ can influence the strength and intermittency of extreme-gradient events, and a systematic investigation of $Pr_M$ effects is also left for future work.

In general, these findings indicate that as the external magnetic field strength increases, highly dissipative small-scale structures become more intense and exhibit reduced dimensionality.

## ACKNOWLEDGMENTS

The authors acknowledge NSFC (Grant No. 12225204), the Department of Science and Technology of Guangdong Province (Grants Nos. 2023B1212060001 and 2020B1212030001), and the Shenzhen Science & Technology Program (Grant No. SYSPG20241211173725008) for financial support. Numerical simulations have been supported by the Center for Computational Science and Engineering of the Southern University of Science and Technology. The participation of YY and WHM was partially supported by NSF Grant No. PHY 2108834.

## AUTHOR DECLARATIONS

### Conflict of Interest

The authors have no conflicts to disclose.

### Author Contributions

**Kai Gao:** Data curation (lead); Formal analysis (lead); Investigation (lead); Writing – original draft (equal). **Bin Jiang:** Data curation (supporting); Formal analysis (supporting); Investigation (supporting); Writing – review & editing (supporting). **Cheng Li:** Data curation (supporting); Investigation (supporting); Methodology (supporting). **Yan Yang:** Conceptualization (supporting); Investigation (supporting); Methodology (supporting); Project administration (supporting); Supervision (supporting); Writing – original draft (equal); Writing – review & editing (equal). **Kangcheng Zhou:** Formal analysis (supporting); Investigation (supporting). **William H. Matthaeus:** Conceptualization (supporting); Investigation (supporting); Supervision (supporting); Writing – original draft (equal); Writing – review & editing (equal). **Sean Oughton:** Investigation (supporting); Writing – review & editing (supporting). **Minping Wan:** Conceptualization (lead); Funding acquisition (lead); Investigation (supporting); Methodology (equal); Project administration (lead); Supervision (lead); Writing – original draft (equal); Writing – review & editing (equal).

## DATA AVAILABILITY

The data that support the findings of this study are available from the corresponding author upon reasonable request.

## REFERENCES

[1] P. Vieillefosse, J. Phys. **43**, 837 (1982).
[2] P. Vieillefosse, Physica A **125**, 150 (1984).
[3] M. S. Chong, A. E. Perry, and B. J. Cantwell, Phys. Fluids A **2**, 765 (1990).
[4] B. J. Cantwell, Phys. Fluids A **5**, 2008 (1993).
[5] A. Perry and M. Chong, Appl. Sci. Res. **53**, 357 (1994).
[6] P. Davidson, *Turbulence: An Introduction for Scientists and Engineers* (Oxford University Press, 2015).
[7] G. Gulitski, M. Kholmyansky, W. Kinzelbach, B. Lüthi, A. Tsinober, and S. Yorish, J. Fluid Mech. **589**, 57 (2007).
[8] C. Meneveau, Annu. Rev. Fluid Mech. **43**, 219 (2011).
[9] B. Lüthi, M. Holzner, and A. Tsinober, J. Fluid Mech. **641**, 497 (2009).
[10] G. Elsinga and I. Marusic, J. Fluid Mech. **662**, 514 (2010).
[11] V. Quattrociocchi, G. Consolini, M. F. Marcucci, and M. Materassi, Astrophys. J. **878**, 124 (2019).
[12] V. Quattrociocchi, G. Consolini, M. Materassi, T. Alberti, and E. Pietropaolo, Chaos, Solitons Fractals: X **9**, 100080 (2022).
[13] E. Jeong and S. S. Girimaji, Theor. Comput. Fluid Dyn. **16**, 421 (2003).
[14] R. K. Bikkani and S. S. Girimaji, Phys. Rev. E **75**, 036307 (2007).
[15] R. Das and S. S. Girimaji, J. Fluid Mech. **895**, A5 (2020).
[16] C. B. da Silva and J. C. Pereira, Phys. Fluids **20**, 055101 (2008).
[17] P. L. Johnson, Phys. Rev. Lett. **124**, 104501 (2020).
[18] D. Buaria, E. Bodenschatz, and A. Pumir, Phys. Rev. Fluids **5**, 104602 (2020).
[19] J. Jiménez, J. Fluid Mech. **409**, 99 (2000).
[20] M. Carbone and A. D. Bragg, J. Fluid Mech. **883**, R2 (2020).

[21]R. M. Pereira, C. Garban, and L. Chevillard, J. Fluid Mech. **794**, 369 (2016).
[22]V. Dallas and A. Alexakis, Phys. Fluids **25**, 105106 (2013).
[23]M. Danish and C. Meneveau, Phys. Rev. Fluids **3**, 044604 (2018).
[24]J. Martın, A. Ooi, M. S. Chong, and J. Soria, Phys. Fluids **10**, 2336 (1998).
[25]J. Lawson and J. Dawson, J. Fluid Mech. **780**, 60 (2015).
[26]P. Bechlars and R. Sandberg, J. Fluid Mech. **815**, 223 (2017).
[27]G. Elsinga and I. Marusic, Phys. Fluids **22**, 015102 (2010).
[28]J. Licon-Salaiz, "Topological aspects of turbulence in the planetary boundary layer," Ph.D. thesis (Universität zu Köln, 2020).
[29]J. Soria and B. Cantwell, *Eddy Structure Identification in Free Turbulent Shear Flows: Selected Papers from the IUTAM Symposium Entitled: "Eddy Structures Identification in Free Turbulent Shear Flows" Poitiers, France, 12–14 October 1992* (Springer, 1993), pp. 379–390.
[30]H. M. Blackburn, N. N. Mansour, and B. J. Cantwell, J. Fluid Mech. **310**, 269 (1996).
[31]L. Wang and X.-Y. Lu, J. Fluid Mech. **703**, 255 (2012).
[32]A. Tsinober, *An Informal Introduction to Turbulence* (Kluwer, 2004), p. 332.
[33]M. Tanaka and S. Kida, Phys. Fluids A **5**, 2079 (1993).
[34]A. Ooi, J. Martin, J. Soria, and M. S. Chong, J. Fluid Mech. **381**, 141 (1999).
[35]F. Liu, Z. Wu, P. Lv, W. Yang, and Y. Zhou, Phys. Fluids **35**, 025138 (2023).
[36]P. Saffman, *Vortex Dynamics*, Cambridge Monographs on Mechanics (Cambridge University Press, 1995).
[37]G. Consolini, V. Quattrociocchi, and M. Marcucci, J. Phys.: Conf. Ser. **1100**, 012007 (2018).
[38]Y. Ji, C. Shen, L. Ma, N. Ren, and N. Ahmad, Phys. Fluids **35**, 025107 (2023).
[39]M.-M. Mac Low, *Turbulence and Magnetic Fields in Astrophysics* (Springer, 2003), pp. 182–212.
[40]H. Politano and A. Pouquet, Phys. Rev. E **52**, 636 (1995).
[41]A. Greco, P. Chuychai, W. Matthaeus, S. Servidio, and P. Dmitruk, Geophys. Res. Lett. **35**, L19111, https://doi.org/10.1029/2008GL035454 (2008).
[42]W.-C. Müller and D. Biskamp, Phys. Rev. Lett. **84**, 475 (2000).
[43]D. Biskamp and W.-C. Müller, Phys. Plasmas **7**, 4889 (2000).
[44]G. Sahoo, P. Perlekar, and R. Pandit, New J. Phys. **13**, 013036 (2011).
[45]G. Sahoo, N. B. Padhan, A. Basu, and R. Pandit, arXiv:2011.04277 (2020).
[46]G. Consolini, M. Materassi, M. F. Marcucci, and G. Pallocchia, Astrophys. J. **812**, 84 (2015).
[47]C. P. Escoubet, M. Fehringer, and M. Goldstein, Ann. Geophys. **19**, 1197 (2001).
[48]B. Hnat, S. Chapman, and N. Watkins, Phys. Rev. Lett. **126**, 125101 (2021).
[49]Y. Yang, W. H. Matthaeus, T. N. Parashar, C. C. Haggerty, V. Roytershteyn, W. Daughton, M. Wan, Y. Shi, and S. Chen, Phys. Plasmas **24**, 072306 (2017).
[50]Y. Yang, W. H. Matthaeus, T. N. Parashar, P. Wu, M. Wan, Y. Shi, S. Chen, V. Roytershteyn, and W. Daughton, Phys. Rev. E **95**, 061201 (2017).
[51]R. Bandyopadhyay, W. H. Matthaeus, T. N. Parashar, Y. Yang, A. Chasapis, B. L. Giles, D. J. Gershman, C. J. Pollock, C. T. Russell, R. J. Strangeway *et al.*, Phys. Rev. Lett. **124**, 255101 (2020).
[52]J. Zhang, S. Huang, F. Sahraoui, N. Andrés, Z. Yuan, K. Jiang, S. Xu, Y. Wei, Q. Xiong, Z. Wang *et al.*, J. Geophys. Res. **128**, e2022JA031064, https://doi.org/10.1029/2022JA031064 (2023).
[53]V. Quattrociocchi, G. Consolini, M. Materassi, A. Verdini, and E. Papini, Chaos, Solitons Fractals **191**, 115900 (2025).
[54]S. Huang, J. Zhang, Q. Xiong, Z. Yuan, K. Jiang, S. Xu, Y. Wei, R. Lin, L. Yu, and Z. Wang, Astrophys. J. **958**, 189 (2023).
[55]Q. Xiong, S. Huang, J. Zhang, Z. Yuan, K. Jiang, H. Wu, R. Lin, L. Yu, and Y. Tang, Geophys. Res. Lett. **51**, e2024GL109356, https://doi.org/10.1029/2024GL109356 (2024).
[56]B. Jiang, C. Li, Y. Yang, K. Zhou, W. H. Matthaeus, and M. Wan, J. Fluid Mech. **974**, A20 (2023).
[57]Y. Yang, M. Linkmann, L. Biferale, and M. Wan, Astrophys. J. **909**, 175 (2021).
[58]S. Oughton, W. Matthaeus, M. Wan, and K. Osman, Philos. Trans. R. Soc., A **373**, 20140152 (2015).
[59]S. Oughton, E. R. Priest, and W. H. Matthaeus, J. Fluid Mech. **280**, 95 (1994).
[60]E. Hameiri and A. Bhattacharjee, Phys. Rev. A **35**, 768 (1987).
[61]S. Banerjee, A. Halder, and N. Pan, Phys. Rev. E **107**, L043201 (2023).
[62]W. H. Matthaeus, J. W. Bieber, and G. P. Zank, Rev. Geophys. **33**, 609, https://doi.org/10.1029/95RG00496 (1995).
[63]J. W. Bieber, W. Wanner, and W. H. Matthaeus, J. Geophys. Res. **101**, 2511, https://doi.org/10.1029/95JA02588 (1996).
[64]R. Bandyopadhyay and D. J. McComas, Astrophys. J. **923**, 193 (2021).
[65]L. Adhikari, G. P. Zank, L.-L. Zhao, and D. Telloni, Astrophys. J. **933**, 56 (2022).
[66]T. N. Parashar and W. H. Matthaeus, Astrophys. J. **832**, 57 (2016).
[67]J. Cho and E. T. Vishniac, Astrophys. J. **539**, 273 (2000).
[68]L. Milano, W. Matthaeus, P. Dmitruk, and D. Montgomery, Phys. Plasmas **8**, 2673 (2001).
[69]M. Wan, S. Oughton, S. Servidio, and W. H. Matthaeus, J. Fluid Mech. **697**, 296–315 (2012).
[70]J. V. Shebalin, W. H. Matthaeus, and D. Montgomery, J. Plasma Phys. **29**, 525–547 (1983).
[71]J. Podesta, Phys. Plasmas **18**, 012906 (2011).